Check for updates

Evidence for three-dimensional spin–velocity alignment in a pulsar

Jumei Yao [1,2 ✉], Weiwei Zhu [1 ✉], Richard N. Manchester[3], William A. Coles [4], Di Li [1,5,6 ✉], Na Wang[2], Michael Kramer [7,8], Daniel R. Stinebring[9], Yi Feng[1], Wenming Yan [2], Chenchen Miao[1], Mao Yuan[1], Pei Wang[1] and Jiguang Lu [1]

More than 50 years after the discovery of pulsars[1] and confirmation of their association with supernova explosions[2-4], the origin of the initial spin and velocity of pulsars remains largely a mystery. The typical space velocities of several hundred km s⁻¹ have been attributed to 'kicks' resulting from asymmetries either in the supernova ejecta or in the neutrino emission[5-7]. Observations have shown a strong tendency for alignment between the pulsar space velocity and the spin axis in young pulsars, but until now these comparisons have been restricted to two dimensions. Here, we report evidence for three-dimensional alignment between the spin and velocity vectors, largely based on observations made with the Five-hundred-meter Aperture Spherical Radio Telescope (FAST) of the pulsar PSR J0538+2817 and its associated supernova remnant S147. Analysis of these and related observations has enabled us to determine the location of the pulsar within the supernova remnant and hence its radial velocity. Current simulations of supernova explosions have difficulty producing such three-dimensional alignment[7-9]. Our results, which depend on the unprecedented sensitivity of the observations, add another dimension to the intriguing correlation between pulsar spin-axis and birth-kick directions, thereby deepening the mysteries surrounding the birth of neutron stars.

PSR J0538+2817 was discovered at Arecibo, and its short period (143 ms) and sky location within the boundary of supernova remnant (SNR) S147 immediately suggested that it was a young pulsar born in the supernova explosion that created S147 (ref. [10]). Modelling of its surrounding X-ray torus structure, with the assumption of alignment between the torus's symmetry axis and the pulsar's spin axis, provided a position angle (PA) (that is, the angle on the sky plane, measured from north towards east) of $\psi_X = 154.0° \pm 5.5°$ and an inclination angle from the line of sight of $\zeta_X = 100° \pm 6°$ into the plane of the sky[11]. Early mean pulse polarization measurements of PSR J0538+2817 gave a value for ζ_{pol} of 97° with large uncertainties[12]; no measurement of ψ_{pol} was reported. Analysis of Very Long Baseline Array observations of PSR J0538+2817 gave an estimated distance of $D = 1,330 \pm 190$ pc and proper motions, referred to the local standard of rest, of $\mu_\alpha = -24.4 \pm 0.10$ mas yr⁻¹ and $\mu_\delta = 57.2 \pm 0.10$ mas yr⁻¹ (refs. [13,14]). These correspond to a PA of $\psi_{pm} = 337.0° \pm 0.1°$, only $3° \pm 6°$ from ψ_X (+180°), which suggests

two-dimensional (2D) alignment. Radial velocities can in principle be determined from pulsar timing observations[15], although no substantial determination has yet been achieved. Optical lines from the binary companion[16] can be used to determine the radial velocity, but the pulsar velocity vector in such a system is essentially unrelated to any natal neutron-star kick.

Through the 'shared-risk' early science program, we observed PSR J0538+2817 on four epochs between 2019 June and 2019 October with the Five-hundred-meter Aperture Spherical Radio Telescope (FAST)[17] by using the central beam of the 19-beam receiver, which covers the frequency band 1,050 MHz to 1,450 MHz. Here, we focus on the October 11 (MJD 58767) observations as they had polarization calibration. For subsequent analyses, we extracted two bands, 1,050–1,150 MHz and 1,350–1,450 MHz, to avoid known radio frequency interference.

The extremely small angular size of the pulsar emission region, coupled with multi-path propagation through an inhomogeneous interstellar electron distribution, produces a complex interference pattern at the observer[18]. As the interference phases are frequency-dependent and there is relative motion between the pulsar, the scattering region and the Earth, we observe a 'dynamic spectrum' with interference maxima or 'scintles' (Fig. 1a). The frequency and timescales of these scintles are strongly frequency-dependent. Analysis of auto-correlation functions and structure functions show that the scintillation is strong and that the short refractive timescale is consistent with daily variations of the turbulence spectrum (Methods and Extended Data Fig. 1).

The 2D power spectrum of each dynamic spectrum, known as the 'secondary spectrum', are shown in Fig. 1b. Both secondary spectra show an arc with a relatively sharp outer boundary and a central bright ridge along the f_ν axis at $f_t = 0$. These scintillation arcs result from interference between the core of the brightness distribution and more highly scattered rays and require dominant scattering in a relatively thin screen along the path[19]. At both frequencies, the arcs show a clear asymmetry about the $f_t = 0$ axis, indicating a persistent phase gradient across the scattering screen[20]. Fitting the more clearly delineated arc at 1,400 MHz with $f_\nu = \eta f_t^2 + \gamma f_t$ results in an arc curvature $\eta = (6.09 \pm 0.10) \times 10^{-4}$ s³ and gradient parameter $\gamma = (4.84 \pm 0.30) \times 10^{-6}$ s² (Extended Data Fig. 2), corresponding to a ray deflection of $\theta_g = 12.1 \pm 0.8$ µas across the scattering disk (see Methods for a full description of the procedure). Given the

[1]National Astronomical Observatories, Chinese Academy of Sciences, Beijing, China. [2]Xinjiang Astronomical Observatory, Chinese Academy of Sciences, Xinjiang, China. [3]CSIRO Astronomy and Space Science, Australia Telescope National Facility, Epping, NSW, Australia. [4]Department of Electrical and Computer Engineering, University of California, San Diego, CA, USA. [5]University of Chinese Academy of Sciences, Beijing, China. [6]NAOC-UKZN Computational Astrophysics Centre, University of KwaZulu-Natal, Durban, South Africa. [7]Max-Planck-Institut für Radioastronomie, Bonn, Germany. [8]Jodrell Bank Centre for Astrophysics, The University of Manchester, Manchester, UK. [9]Department of Physics and Astronomy, Oberlin College, Oberlin, OH, USA. ✉e-mail: yaojumei@xao.ac.cn; zhuww@nao.cas.cn; dili@nao.cas.cn
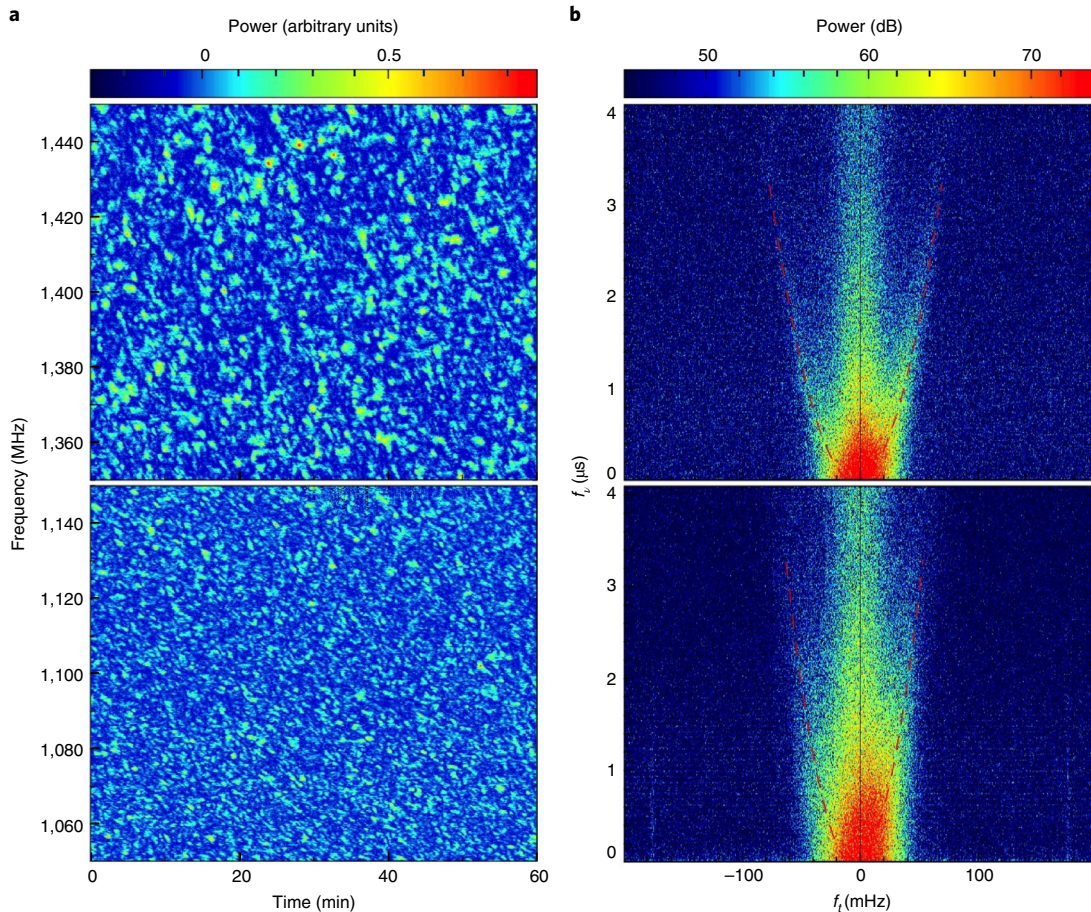
Fig. 1 | Dynamic spectra and secondary spectra of PSR J0538+2817. a,b, Lower panels show dynamic spectrum and secondary spectrum for 100 MHz bands centred at 1,100 MHz. Upper panels show dynamic spectrum and secondary spectrum for 100 MHz bands centred at 1,400 MHz. For the dynamic spectra (**a**), the colour scale is linear in signal power with arbitrary units. The secondary spectra (**b**) are shown with a logarithmic (dB) colour scale. The horizontal and vertical axes are conjugate time (f_t) and conjugate frequency (f_ν). The red dashed lines in **b** represent the best-fit parameters of the arc, with the derived η and γ values scaled by $(1{,}400/1{,}100)^2$ and $(1{,}400/1{,}100)^3$, respectively, for the 1,100 MHz plot.

estimated distance to the pulsar and SNR, the derived pulsar–screen distance is $D_{\mathrm{ps}} = 32.1 \pm 7.1\,\mathrm{pc}$, which is consistent with the radius $R_{\mathrm{s}} = 32.1 \pm 4.8\,\mathrm{pc}$ of SNR S147 and strongly suggests that the scattering screen is located on the near side of the SNR shell (Methods and Extended Data Fig. 3).

As Extended Data Fig. 4 shows, η is stable within the uncertainties across the four observational epochs, but γ varies considerably across intervals as short as one day. These results will be discussed in a future paper. Based on simulations, we attribute the rare central ridges observed for PSR J0538+2817 to scattering by asymmetric structures in the screen (Methods and Extended Data Fig. 5).

In Fig. 2, we show the polarization profile of PSR J0538+2817 derived from the FAST observations in the band 1,350–1,450 MHz. We derived the best-fit pulsar rotation measure (RM) by fitting the observed PAs across both observed FAST bands, 1,050–1,150 MHz and 1,350–1,450 MHz, to give $\mathrm{RM} = +39.56 \pm 0.14\,\mathrm{rad\,m^{-2}}$. The red line in the middle panel of Fig. 2 represents the best-fit rotating vector model (RVM)[21] applied to the observed PA variations (Methods), and the top panel shows the corresponding fit residuals as a function of pulse phase. To compare ψ_{pol} with other determinations of the PAs of the projected spin axis and pulsar velocity, we must correct it to infinite frequency to give the so-called 'intrinsic' PA of the spin axis. By using the RM given above, we obtain ψ_{pol}(in

trinsic) $= -18.5° \pm 1.7°$. The polarization fitting gives an inclination angle of the pulsar spin axis to the line of sight of $\zeta_{\mathrm{pol}} = 118.5° \pm 6.3°$.

Figure 3 illustrates the three-dimensional (3D) relationship of the derived pulsar velocity and spin vectors. On the plane of the sky, the position angle offset between the projected velocity and spin axis estimated from polarization PA fitting, $\Delta\Psi_{\mathrm{pm\_pol}} = 4.5° \pm 1.7°$, is consistent with that from modelling of the X-ray torus, $\Delta\Psi_{\mathrm{pm\_X}} = 3.0° \pm 5.8°$, further confirming approximate 2D alignment. The inclination angles of the velocity and spin vectors are less well determined. With the assumption that the scattering is dominated by the SNR shell and that the shell is spherical, we find that the pulsar is located $2.9^{+5.6}_{-5.4}$ pc behind the plane of the sky. This corresponds to a pulsar radial velocity of $81^{+158}_{-150}\,\mathrm{km\,s^{-1}}$ and an inclination angle of the pulsar velocity of $\zeta_\nu = 110°\,^{+16°}_{-29°}$. This inclination angle overlaps well within 68% confidence intervals with both ζ_{pol} measured from FAST polarization ($\Delta\zeta_{\nu\_\mathrm{pol}} = 9°\,^{+17°}_{-30°}$) and ζ_{X} measured from the X-ray torus modelling ($\Delta\zeta_{\nu\_\mathrm{X}} = 10°\,^{+17°}_{-30°}$). In Fig. 3b, we show the 3D relationships of the vectors with 68% and 95% confidence limit in their orientation. As Fig. 3 illustrates, the inclination angles for the spin vector derived from the pulse polarisation measurements and the X-ray torus measurements differ at about the 2σ level. We do not consider this difference to be notable given the possibility of unrecognized systematic errors in either or both measurements.
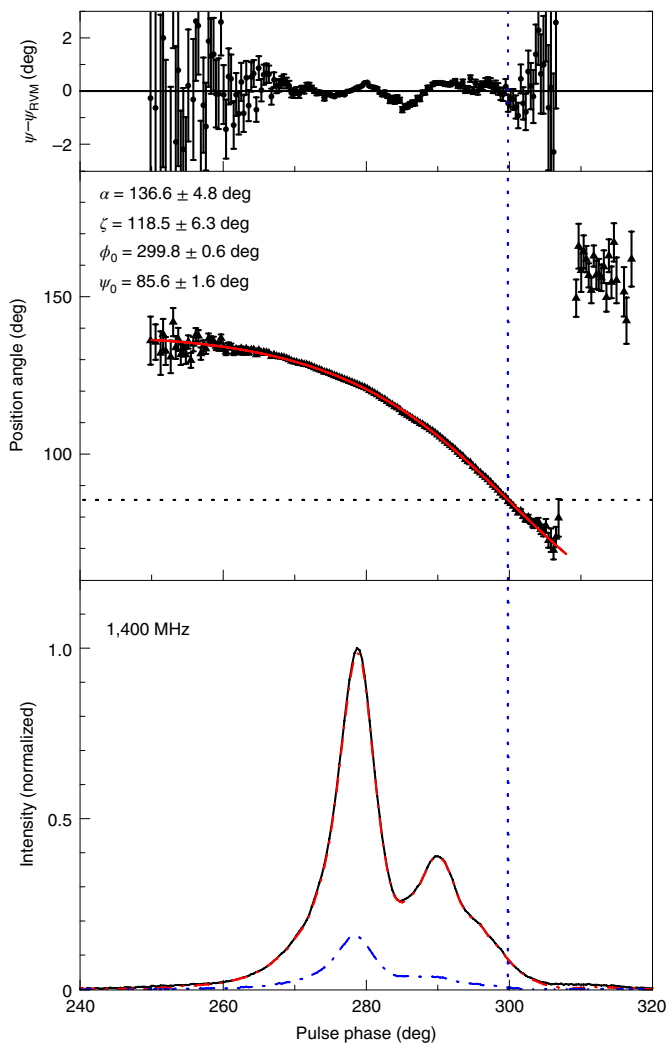
Fig. 2 | Polarization profile of J0538+2817 at 1,400 MHz. The bottom panel shows the total intensity (solid black line), the linear polarization (red dash-dot line) and circular polarization (blue dash-dot line). The middle panel shows the observed position angles ψ at 1,400 MHz as a function of pulse phase; the error bars are $\pm 1\sigma$ and the red line gives the best-fit RVM solution. The top panel shows the fit residuals, again with $\pm 1\sigma$ error bars. The vertical dotted line shows the central pulse phase of the RVM fit, ϕ_0, and the horizontal dotted line gives the corresponding PA at 1,400 MHz, ψ_0. Best-fit parameters with 1σ uncertainties from the RVM fit are given in the middle panel.

Approximate 2D spin–velocity alignment has been demonstrated for more than 30 mostly young pulsars[22,23]. However, in this paper we demonstrate the 3D alignment of a pulsar's spin and space-velocity vectors. The importance of this result is illustrated in Fig. 4, which compares the constraints on the relative alignment of the spin and velocity vectors with and without the knowledge of the measured pulsar radial velocity. For the latter, following Dinçel et al.[14], we assume a uniform distribution between $-1{,}500\,\mathrm{km\,s^{-1}}$ and $+1{,}500\,\mathrm{km\,s^{-1}}$. With this assumed radial velocity distribution, the distribution of Θ_{3D} based on the FAST polarization results (Fig. 4, red) has a large 68% confidence interval of about 74°. For the X-ray torus results, the distribution (Fig. 4, magenta) is also broad with a 68% confidence interval of about 68°. Including the observed constraint on ζ_v strongly constrains the 3D angle between the spin axis measured from FAST polarization and the velocity vector with a clear peak around 6° and a 68% probability of being less than 28°.

From the X-ray torus modelling there is a peak around 10° and the angle is smaller than 23° with 68% probability. It is clear that the observational constraints strongly limit the range of possible misalignment angles. For the polarization results, the low probability of misalignment angles less than 4° results from the tight constraint on the position angle of the transverse velocity from the proper-motion results of the very long baseline interferometry (VLBI) (Fig. 3a, left).

Existing models struggle to explain the spin–velocity 3D alignment that we have observed for PSR J0538+2817 and that is commonly assumed for other pulsars based on the 2D alignment. For example, the electromagnetic rocket model[24] invokes a post-natal acceleration along the pulsar's spin axis by an asymmetric radiation–reaction force from an offset magnetic dipole. This model does result in spin–velocity alignment, but requires a very high initial neutron-star spin rate (>1 kHz), which is unlikely for PSR J0538+2817, especially given its long inferred initial spin period of 140 ms (ref. [12]). Numerical modelling of supernova explosions to determine the explosion energetics and the properties of any compact remnant has been carried out for decades. Initially such modelling was one-dimensional (1D), then 2D and more recently 3D, with a wide variety of numerical codes emphasizing different aspects of the explosion and making different approximations[25]. In general, 3D models do not include rotation of the progenitor star, as rapidly spinning iron cores are not expected for the majority of supernova progenitors[26]. In these simulations, neutron-star kicks could result from asymmetries in the ejecta (for example, the 'tug-boat' mechanism) or in the neutrino emission, and spins result from fall-back of ejecta onto the neutron star[6,7]. In these models, there is little or no relationship between the neutron-star kick direction and spin axis and hence no tendency for an alignment. Possible mechanisms for spin–velocity alignment include ejecta directed by the rotation of the progenitor star[6,7,9], neutrino emission preferentially channelled along the rotation axis[27] and random torques averaged over several rotation periods of the proto-neutron star producing a net 'slow kick' along the spin axis[27,28], but there is no generally accepted explanation.

It is also clear that the alignment is not perfect. Based on existing 2D spin–velocity alignment detections, small but notable misalignments of 5°–10° have been observed in many pulsars, including PSR J0538+2817. These misalignments could result from break-up of a pre-supernova binary system[14] or from stochastic variations in the direction of the natal kick or spin-up torques[6,7] and are an important diagnostic of the processes involved. Systematic measurements of the 3D orientations of pulsar spin and velocity vectors, building on the present work, are therefore highly desirable. With its great sensitivity, FAST is poised to play an important role in these investigations.

Methods

Observations and data processing. The polarization response was calibrated by using short observations of a pulsed noise source injected into the feed before and after the pulsar observation. As the observations were at low zenith angle, the system temperature $T_{sys} \leq 20\,\mathrm{K}$, which, combined with the system gain of $\sim 16\,\mathrm{K\,Jy^{-1}}$ (ref. [29]), enabled a single pulse detection threshold of 0.25 mJy (5σ). A digital filterbank system was used to form and record the full polarization data sampled at 49.152 μs intervals with 3,277 channels of bandwidth of 0.122 MHz across the analysed 400 MHz band from 1,050 MHz to 1,450 MHz. We used the DSPSR analysis program[30] and the PSRCHIVE software package[31] to reduce our data. Data for each channel were folded according to the pulsar period by using a sub-integration time of 2.5 s and then the polarization was calibrated.

Interstellar scintillation data analysis. For the interstellar scintillation (ISS) analysis, we first formed total intensity (Stokes I) profiles for each channel and sub-integration, did further radio frequency interference (RFI) rejection by using PAZI and then used PSRFLUX to form the dynamic spectrum. To remove the effects of short-term pulse intensity variations, we normalized the mean power of each sub-integration spectrum to the mean power across the observation. To compute the secondary spectra, we applied a Hamming window function to the outer 10% of each dynamic spectrum to reduce the effects of aliasing in the
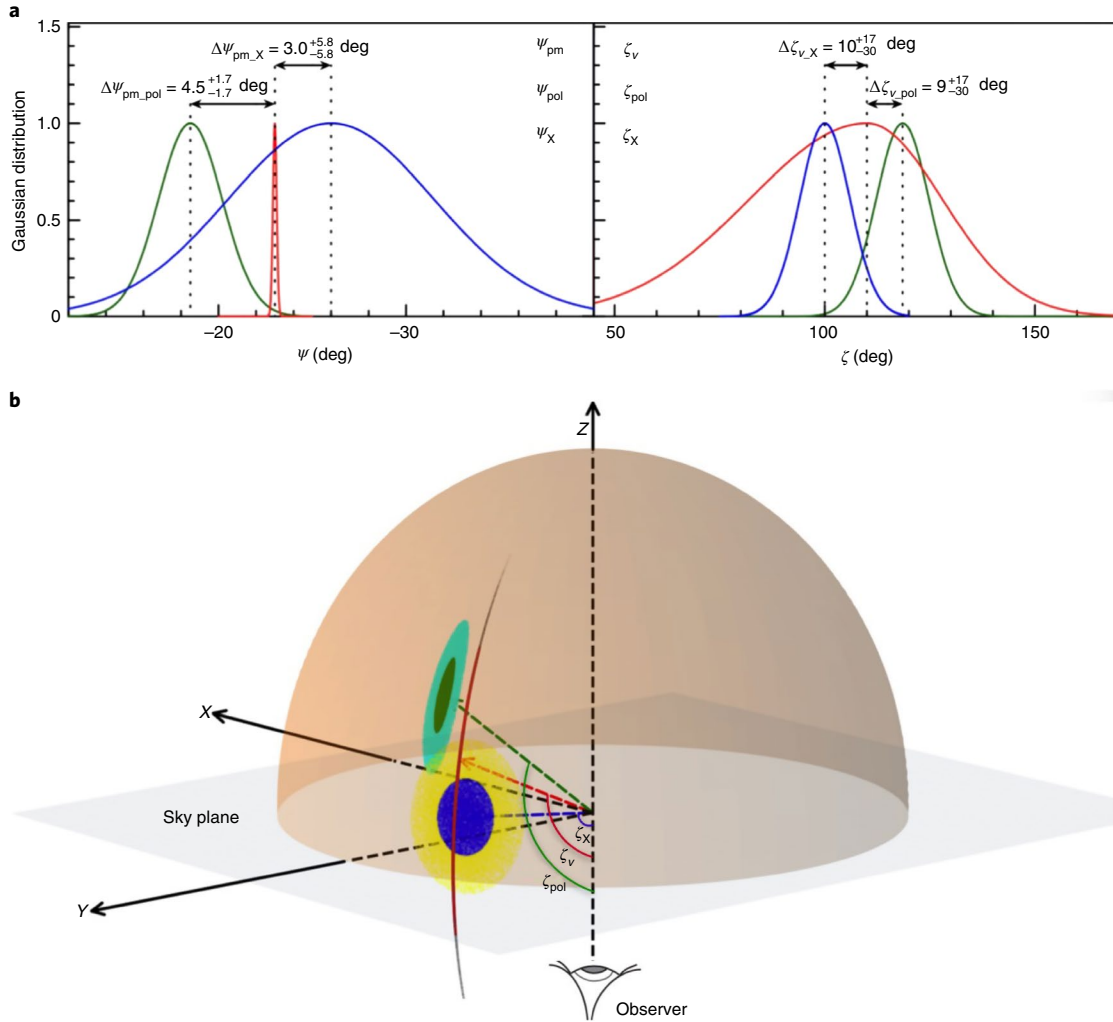
Fig. 3 | Position angles and inclination angles of the spin axis and velocity vector and the corresponding 3D distribution on the surface of a unit sphere.
a, The spin-vector constraints estimated from polarization PA fitting and X-ray torus fitting are shown in dark green and blue, respectively, and the velocity-vector constraints obtained from VLBI (position angle) and the ISS analysis (inclination angle) are shown in red. The differences between the position angle and the inclination angle of the spin axis and velocity vector are showed with 1σ uncertainties. **b**, The 3D constraints with 68% and 95% confidence limit for the vector orientations, in dark green and light green for the spin obtained from PA fitting, in blue and yellow for the spin given by X-ray torus fitting, and in red and grey for the velocity, with the inclination angles marked.

secondary spectrum. As the scintillation fluctuation spectrum is typically steep, we used first-differences to pre-whiten the dynamic spectrum[32]. After this, we formed the secondary spectrum by using a 2D Fourier transform, took its squared magnitude and finally applied the appropriate post-darkening filter to recover our best estimate of the secondary spectrum. The Nyquist frequencies corresponding to the 2.5 s sub-integration time and the 0.122 MHz channel bandwidth are $f_t(\text{Nyquist}) = 200\,\text{mHz}$ and $f_\nu(\text{Nyquist}) = 4.1\,\mu\text{s}$, respectively.

Polarization data analysis. For the polarization analysis, we summed the 60-minute observation over time to form a single calibrated polarization profile for each channel. By using the PSRCHIVE program RMFIT, we derived the best-fit pulsar RM by fitting the observed PAs across both observed FAST bands, 1,050–1,150 MHz and 1,350–1,450 MHz, and obtained $\text{RM} = +39.56 \pm 0.14\,\text{rad}\,\text{m}^{-2}$. This is quite different from the previously published value of $\text{RM} = -7 \pm 12\,\text{rad}\,\text{m}^{-2}$ (ref. [33]). We have no explanation for this difference, but we are confident that our measurement accurately gives the RM at the time of the FAST observations. In the RVM convention, the PA as a function of pulse longitude, ϕ, can be expressed as

$$\psi = \psi_{\text{pol}} + \arctan \frac{\sin \alpha \sin(\phi - \phi_0)}{\sin \zeta \cos \alpha - \cos \zeta \sin \alpha \cos(\phi - \phi_0)}, \quad (1)$$

where ϕ_0 is the pulse phase for the closest approach of the line of sight to the magnetic axis, with a corresponding PA of ψ_{pol}. In the simple dipolar model, ψ_{pol} is the position angle of the pulsar spin axis, α is the angle between the spin axis and

magnetic axis, and ζ is the inclination angle of the spin axis from the line of sight. Choosing data from the 1,350–1,450 MHz band, we then fitted the RVM model to the PA variation across the profile by using PSRMODEL; the resulting fit is shown in Fig. 2. The fit residuals shown in the upper panel are very close to zero across the two main pulse components (where the signal-to-noise ratio is sufficient). However, there are notable deviations in the region where the two components overlap, suggesting that the two components come from (slightly) different source regions. Mixing of the radiation from the two regions could result in the observed small deviations in the resultant PA in the overlap region.

To compare ψ_{pol} with other determinations of the PAs of the projected spin axis and pulsar velocity, we must correct it to infinite frequency to give the so-called 'intrinsic' PA of the spin axis. By using the RM given above, we obtain $\psi_{\text{pol}}(\text{intrinsic}) = -18.5° \pm 1.7°$. The inclination angle of the pulsar spin axis to the line of sight needs no correction and is $\zeta_{\text{pol}} = 118.5° \pm 6.3°$. The derived inclination angle of the magnetic axis relative to the spin axis is $\alpha = 136.6° \pm 4.8°$, which implies a minimum angle between the magnetic axis and the line of sight $\beta = \alpha - \zeta = 18.1° \pm 7.9°$ with an 'outer' line of sight, that is, passing on the equatorial side of the magnetic axis[34]. Note that our analysis uses the International Astronomical Union convention of PA increasing in a counter-clockwise direction on the sky. As PSRMODEL uses the opposite sense for PA, we have used conversion equations to obtain a consistent set of parameters[35].

Auto-correlation function and structure function analysis. We form 2D auto-correlation functions (ACFs) of the intensity fluctuations, $\rho_{\text{int}}(\tau, \nu)$, and then
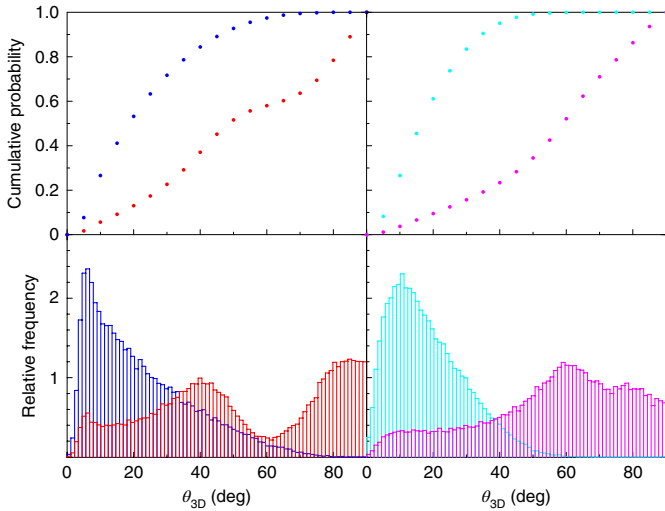
Fig. 4 | The cumulative and relative distributions of the spin–velocity misalignment angle Θ_{3D}. The Θ_{3D} values satisfy the constraints on ψ and ζ shown in Fig. 3, based on a random selection of 3D orientations for the spin, velocity and line-of-sight directions. Spin-vector constraints estimated from polarization PA fitting are shown in the left panels and from X-ray torus fitting are shown in the right panels. For the red and magenta distributions, we ignore the observational constraints on the radial velocity and assume a uniform distribution between −1,500 km s⁻¹ and +1,500 km s⁻¹. The blue and cyan distributions include all constraints shown in Fig. 3.

estimate the diffractive time and frequency scales, $\Delta\tau_d$ and $\Delta\nu_d$ respectively. As $\rho_{int}(\tau,\nu)$ shows a skewness resulting from a phase gradient across the scattering disk, the frequency widths are somewhat biased. Hence, we can only determine approximate scintillation bandwidths $\Delta\nu_d$ from the 2D ACF $\rho_{int}(\tau,\nu)$, giving values of 0.40 MHz and 0.86 MHz at 1,100 MHz and 1,400 MHz, respectively. The scintillation strength u, defined as $u = \sqrt{\nu/\Delta\nu_d}$ (ref. [18]), is 52 and 40 respectively, indicating that the scintillation is very strong in both observational bands.

A cut through the temporal axis of the ACF, $\rho_{int}(\tau,0)$, is independent of any phase gradient and hence can be used to estimate the phase structure function $D_\phi(\tau)$ and the power spectrum of the turbulence. The canonical problem in small-angle forward scattering from a thin phase screen is appropriate for cases of interstellar scintillation in which the scattering plasma occupies a small fraction of the line of sight. We consider a plane wave in free space propagating in the z direction incident on a thin slab of material of thickness δz with a refractive index $n(x,y,0) \neq 1$. On passing through this slab the electric field is $E(x,y,0) = \exp(-j\phi(x,y))$ (where j indicates the imaginary part), where $\phi(x,y) = kn(x,y,0)\delta z$, wavenumber $k = 2\pi/\lambda$ and λ is the wavelength. This field can be expressed as an angular spectrum of plane waves by taking the 2D Fourier transform of $E(x,y)$.

$$\tilde{E}(\kappa_x, \kappa_y) = \int \int E(x,y) \exp(-j(\kappa_x x + \kappa_y y)) \mathrm{d}x \, \mathrm{d}y. \tag{2}$$

Here the plane waves are described by $\kappa_x = k\sin(\theta_x)$ and $\kappa_y = k\sin(\theta_y)$. The ACF of the electric field, which is called the 'mutual coherence function' in statistical optics, is given by

$$\rho_e(s_x, s_y, z = 0) = \langle \exp(-j(\phi(x,y) - \phi(x+s_x, y+s_y))) \rangle \tag{3}$$

where $\phi(x,y)$ and $\phi(x+s_x, y+s_y)$ are the plasma phase contribution at transverse coordinates **r** and **r+s**, respectively. If $\phi(x,y)$ is a Gaussian random process, then

$$\rho_e(s_x, s_y, z = 0) = \exp(-0.5\langle(\phi(x,y) - \phi(x+s_x, y+s_y))^2\rangle). \tag{4}$$

The argument of the exponential is called the phase structure function $D_\phi(s_x, s_y)$. If the power spectrum of $\phi(x)$ follows a power law of $\sim \kappa_x^{-\alpha}$ with $\alpha < 4$, then the structure function follows a power law of $\sim s_x^{\alpha-2}$. Thus, a measurement of $D_\phi(s_x, s_y)$ provides an estimate of the spectral exponent (for which the Kolmogorov value is 11/3). The Fourier transform of $\rho_e(s_x, s_y)$ is the angular power spectrum $B(\theta_x, \theta_y)$. The plane wave changes phase as it propagates to the observer but it does not change amplitude. Therefore, $B(\theta_x, \theta_y)$ does not change as the angular spectrum propagates from the slab to the Earth, and $\rho_e(s_x, s_y)$ cannot change either. Thus, $\rho_e(s_x, s_y)$ could be measured at the Earth and it would still be defined by $D_\phi(s_x, s_y)$.

In general, one would need an interferometer to measure $\rho_e(s_x, s_y)$ at the Earth (where it would be called the 'visibility'). However, as the wave propagate from the slab to the observer, the fluctuations in $E(x,y)$ develop amplitude fluctuations. When these are 'strong' enough, $E(x,y)$ becomes a 2D Gaussian random variable. It is much easier to measure the intensity than the complex electric field, and in this case we have $\rho_{int}(s_x, s_y) = |\rho_e(s_x, s_y)|^2$. Normally, we measure intensity $I(t) = I(x = Vt)$ and therefore $\rho_{int}(\tau) = |\rho_e(V\tau, 0)|^2$, where V is the transverse velocity of the 'line of sight' with respect to the plasma. Hence, we obtain the expression

$$D_\phi(\tau) = -\log_e[\rho_{int}(\tau)] \tag{5}$$

to derive the phase structure function $D_\phi(\tau)$ from the 1D temporal intensity ACF $\rho_{int}(\tau)$.

To accurately determine $\rho_{int}(\tau)$ for each band, we divide the dynamic spectra into 10 sub-bands, each 10 MHz wide, form the time-domain ACF for each, and then average these to get the mean ACF for each band. The zero-lag (or total power) point on these ACFs includes a white noise contribution, mainly from receiver noise. This white noise contribution was estimated by removing power from the zero-lag ACF component until the peak of the ACF was approximately Gaussian and then by renormalizing the ACF. After this correction, $D_\phi(\tau)$ was approximately linear (on log–log axes) at small τ.

In Extended Data Fig. 1 the upper panels show 1D ACFs for the two bands for observations on two consecutive days, 2019 October 10 and 11. The white noise spikes in the ACFs before correction were, for MJD 58766, 11.0% and 9.1% of the total power at 1,100 and 1,400 MHz, respectively, and for MJD 58767, 4.8% and 6.1% of the total power. By using a Gaussian function to fit the peak of the ACFs for MJD 58767, we find that the scintillation timescales $\Delta\tau_d$ at 1,100 and 1,400 MHz are 19.1 ± 0.3 and 29.1 ± 1.1 s, respectively. These uncertainties include two parts, the statistical uncertainty from the data fitting and the fractional uncertainty from the finite number of observed scintles in the dynamic spectra[36,37].

Phase structure functions corresponding to these ACFs are shown in the lower panels of Extended Data Fig. 1. There, we scaled $D_\phi(\tau)$ by $(1,100/1,400)^2$ for the 1,100 MHz band, to make the comparison with $D_\phi(\tau)$ at 1,400 MHz exact. For MJD 58767, the fitted slopes for both bands are broadly consistent with the expected Kolmogorov exponent of 5/3 for $\tau < 20$ s, but there is a suggestion of flattening at longer time lags in the 1,400 MHz data, which is more reliable at longer time lags. This flattening is much more prominent in the observations for MJD 58766 on the previous day (Extended Data Fig. 1, lower left panel), and the fitted slopes of ~1.2 are inconsistent with a Kolmogorov fluctuation spectrum. The timescale for the line of sight to cross the scattering disc (the refractive timescale) is $\Delta\tau_r = u^2\Delta\tau_d$ and is therefore about 14.3 h at 1,100 MHz and 12.9 h at 1,400 MHz. Consequently, daily variations of the turbulence spectrum are consistent with the estimated refractive timescale.

Arc curvature fitting. Scintillation arcs may be described by the equation

$$f_\nu = \eta f_t^2 + \gamma f_t, \tag{6}$$

where η is the arc curvature and γ represents a phase slope across the scattering disk[20]. To estimate η and γ we use the more clearly delineated asymmetric arc at 1,400 MHz. We first randomly generate 5,000 pairs of (η, γ) over the ranges $\eta = 4.6 \times 10^{-4}$ s³ to 7.6×10^{-4} s³ and $\gamma = -5 \times 10^{-6}$ s² to 15×10^{-6} s². Each (η, γ) corresponds to an arc in the secondary spectrum. We then sample the outer parts of each arc ($f_t \in [-80 \text{ mHz}, -40 \text{ mHz}]$ and $[40 \text{ mHz}, 80 \text{ mHz}]$) with 350 points on each side, taking the nearest point in the secondary spectrum to each point along the arc, weighting it by its normalized power and forming the summed weighted power for that arc. We then use a 2D Gaussian function to fit the relatively symmetric peak of the arc power distribution over the ranges $\eta = 5.4 \times 10^{-4}$ s³ to 6.8×10^{-4} s³ and $\gamma = 1 \times 10^{-6}$ s² to 9×10^{-6} s² (Extended Data Fig. 2), which results in the following best estimates for η and γ:

$$\eta = (6.09 \pm 0.10) \times 10^{-4} \text{ s}^3 \tag{7}$$

and

$$\gamma = (4.84 \pm 0.30) \times 10^{-6} \text{ s}^2. \tag{8}$$

The quoted uncertainties are calculated by dividing the 60-minute observation into four 15-minute blocks, separately fitting for η and γ by using the procedure described above for each block, and taking one half of the r.m.s. deviation about the mean as the uncertainty in each parameter.

For f_ν and f_t, we have

$$f_\nu = \frac{D(1-s)}{2cs}(\theta^2 + 2\theta\theta_g) \tag{9}$$

and

$$f_t = \frac{2\pi\nu_c V_{\text{eff},\perp}}{cs}\theta, \tag{10}$$

where c is the speed of light, ν_c is the band-centre frequency, θ is the ray deflection angle, θ_g is the refractive angle of the wave front, and the scattering screen is located at a distance sD from the pulsar[20]. The effective perpendicular (or transverse) velocity is given by

$$V_{\mathrm{eff},\perp} = (1-s)V_{\mathrm{psr},\perp} + sV_{\mathrm{Earth},\perp} - V_{\mathrm{scr},\perp}, \tag{11}$$

where $V_{\mathrm{psr},\perp}$ is the pulsar transverse velocity obtained from the measured proper motion, $V_{\mathrm{Earth},\perp}$ is the component of the Earth's velocity perpendicular to the line of sight to the pulsar and $V_{\mathrm{scr},\perp}$ is the component of the velocity of the scattering screen perpendicular to the line of sight. After correcting the pulsar proper motion to the local standard of rest[14] and taking the pulsar distance of 1,330 pc, the pulsar perpendicular velocity ($V_{\mathrm{psr},\perp}$) is $391 \pm 56\,\mathrm{km\,s^{-1}}$. Even with correction to the local standard of rest, the Earth's space velocity is $\lesssim 30\,\mathrm{km\,s^{-1}}$. We can therefore safely neglect the Earth's velocity in equation (11) (especially because, as we show below, s is small). Although we are not sure of the exact location or identity of the scattering screen, there is an abundance of filaments located in the expanding gas behind the outer shock that are good candidates for the scattering screen. These filaments have an expansion velocity of about $80\,\mathrm{km\,s^{-1}}$ with a scatter of the order of $20\,\mathrm{km\,s^{-1}}$ (ref. [38]), and the perpendicular component of this is $35 \pm 9\,\mathrm{km\,s^{-1}}$. Including this term, we have

$$V_{\mathrm{eff},\perp} \approx (1-s)V_{\mathrm{psr},\perp} - V_{\mathrm{scr},\perp}, \tag{12}$$

$$\eta = 4,625\,\frac{D_{\mathrm{kpc}}s(1-s)}{\nu_{\mathrm{GHz}}^2[(1-s)V_{\mathrm{psr},\perp} - V_{\mathrm{scr},\perp}]^2} \tag{13}$$

and

$$\gamma = 0.1496\,\frac{D_{\mathrm{kpc}}\theta_{g,\mathrm{mas}}(1-s)}{\nu_{\mathrm{GHz}}^2[(1-s)V_{\mathrm{psr},\perp} - V_{\mathrm{scr},\perp}]}, \tag{14}$$

where velocities are in $\mathrm{km\,s^{-1}}$. Taking $\nu = 1.4\,\mathrm{GHz}$ and assuming Gaussian distributions for the measured values of $V_{\mathrm{psr},\perp}$, $V_{\mathrm{scr},\perp}$, η, γ and D in equations (13) and (14), we obtain the distributions of θ_g and s by using a Monte Carlo analysis. Then we fit the distributions with Gaussian functions having different widths on the two sides, and find that

$$\theta_g = 12.1 \pm 0.8\,\mathrm{\mu as}, \tag{15}$$

and

$$s = 0.0241 \pm 0.0041. \tag{16}$$

The uncertainty in s is dominated by the uncertainty in the pulsar distance. This contributes 93% of the total uncertainty, compared to 6% from the uncertainty in screen velocity and 1% from the uncertainty in the measured scintillation arc curvature and pulsar proper motion.

This determination of s is based on observations made on MJD 58767. As mentioned previously, scintillation observations of J0538+2817 were also made at three earlier epochs. The results from all observations are summarized in Extended Data Fig. 4. This table shows that the arc curvature η is relatively stable over the 132 days covered by these observations, with an r.m.s. scatter of $0.08 \times 10^{-4}\,\mathrm{s^3}$, which is consistent with the uncertainty of each measurement. This corresponds to a variation in ζ_v of less than 5°. Conversely, the arc asymmetry γ and hence the refractive angle θ_g vary greatly from epoch to epoch. These time variations and their implications will be discussed in a future publication.

Substituting for the measured values, the pulsar–screen distance $D_{\mathrm{ps}} = sD$ is 32.1 ± 7.1 pc. The uncertainty in D_{ps} is given by

$$\delta D_{\mathrm{ps}} = \sqrt{D^2\,\delta s^2 + s^2\,\delta D^2}, \tag{17}$$

where δs and δD are the uncertainties in s and D, respectively. As with s, the dominant contribution to δD_{ps} is the uncertainty in D (96%).

Association between PSR J0538+2817 and SNR S147. S147 is an almost circular SNR of radius $\theta_s = 83' \pm 3'$ (ref. [39]) located in the Galactic anti-centre region with geometric centre at $\alpha_{\mathrm{snr}} = 05\,\mathrm{h}\,40\,\mathrm{min}\,01\,\mathrm{s} \pm 2\,\mathrm{s}$, $\delta_{\mathrm{snr}} = +27°\,48'\,09'' \pm 20''$ (J2000) (ref. [12]). PSR J0538+2817 is located at $\alpha_{\mathrm{psr}} = 05\,\mathrm{h}\,38\,\mathrm{min}\,25.0572\,\mathrm{s}$, $\delta_{\mathrm{psr}} = +28°\,17'\,09.161''$ (J2000) (ref. [13]). The angular offset of the pulsar from the SNR centre, θ_p, is given by

$$\theta_p^2 = (\alpha_{\mathrm{snr}} - \alpha_{\mathrm{psr}})^2 \cos^2\delta_{\mathrm{snr}} + (\delta_{\mathrm{snr}} - \delta_{\mathrm{psr}})^2, \tag{18}$$

that is, $\theta_p = 35.9' \pm 0.4'$. Based on extinction in associated dust clouds, the estimated distance to S147 is $1,220 \pm 210$ pc (ref. [40]), which is consistent with the VLBA pulsar distance of $1,330 \pm 190$ pc (ref. [13]) and gives a physical radius for the SNR of $R_s = D\theta_s = 32.1 \pm 4.8$ pc.

Within the uncertainties, this is equal to the estimated pulsar–scattering screen distance of $D_{\mathrm{ps}} = 32.1 \pm 7.1$ pc derived above, which strongly suggests that the

scattering screen can be identified with the near side of the SNR shell and that the pulsar is within the shell. However, it is possible (although unlikely) that the pulsar could be behind the SNR and that the scattering screen causing the observed arc is the far side of the SNR shell. In this case, we might also expect to see scattering from the near side of the shell, about 100 pc from the pulsar. There is no evidence for such a second arc, which supports the idea that the pulsar is located within the shell and that the scintillation arc results from scattering in the near side of the SNR shell.

Overall, there is a low probability ($\sim 3 \times 10^{-4}$) of having a random young pulsar such as PSR J0538+2817 pass so close to the centre of S147 and not be associated at birth[22]. These arguments together with the strong evidence presented above that the pulsar lies within the SNR shell and is scattered by it make the case for the physical association of PSR J0538+2817 and SNR S147 overwhelming.

Calculation of the inclination angle. To compute ζ_v, the inclination angle of pulsar velocity vector from the observer, we adopt a coordinate system with the geometry shown in Extended Data Fig. 3 with assumptions that SNR S147 is a perfectly spherical SNR and that the scattering screen is located exactly at the outer edge of the SNR shell, that is $r = R_s$. From the right-triangle OKS, we have

$$(D_{\mathrm{ps}} - z_p)^2 + x_p^2 + y_p^2 = R_s^2. \tag{19}$$

Solving this for z_p and neglecting the unphysical solution, we have

$$z_p = D_{\mathrm{ps}} - \sqrt{R_s^2 - x_p^2 - y_p^2} = D\left(s - \sqrt{\theta_s^2 - \theta_p^2}\right) = D\,\theta_z, \tag{20}$$

where we define the dimensionless scale factor θ_z. Assuming Gaussian distributions for the input parameters, we get the distribution of z_p by using a Monte Carlo analysis. Following the same procedure used for estimating θ_g and s, we obtain

$$z_p = 2.9^{+5.6}_{-5.4}\,\mathrm{pc}. \tag{21}$$

As we can assume that PSR J0538+2817 was born at the centre of SNR S147, we have $V_z = z_p/\tau_k$ where τ_k is the kinematic age. Given the improved proper-motion measurements[13], we estimate a revised kinematic age of $\tau_k = 34.8 \pm 0.4$ kyr, and obtain the pulsar radial velocity

$$V_z = 81^{+158}_{-150}\,\mathrm{km\,s^{-1}} \tag{22}$$

and a total space velocity

$$V = 407^{+79}_{-57}\,\mathrm{km\,s^{-1}}. \tag{23}$$

From triangle OPS, by using the law of cosines and defining Θ_p, we obtain

$$\zeta_v = 180° - \arccos\left(\frac{D_{\mathrm{op}}^2 + D_{\mathrm{ps}}^2 - R_s^2}{2\,D_{\mathrm{op}}\,D_{\mathrm{ps}}}\right) = 180° - \arccos\left(\frac{\Theta_p^2 + s^2 - \theta_s^2}{2\,s\,\Theta_p}\right), \tag{24}$$

where

$$D_{\mathrm{op}}^2 = x_p^2 + y_p^2 + z_p^2 = D^2\left(\theta_p^2 + \theta_z^2\right) = D^2\,\Theta_p^2. \tag{25}$$

Again following the procedure for estimating the uncertainty in θ_g and s, we obtain

$$\zeta_v = 110°\,^{+16°}_{-29°} \tag{26}$$

for the inclination angle of the pulsar velocity vector.

We note that the uncertainty in z_p, and hence in V_z and ζ_v, is dominated by the uncertainty in the distance D to the pulsar (and to the SNR). This contributes about 87% of the uncertainty in z_p. The derived value of z_p also depends on the assumptions that the scattering is dominated by a thin screen located at the boundary of a spherical SNR. As discussed in the previous section, filamentary structure in the shocked gas immediately behind the outer shock is a very plausible location for the scattering screen. The Hα images of S147 (ref. [38]) suggest that most of the filaments lie close to the outer boundary of the shell, perhaps within about 10% of the boundary radius. The estimated fractional uncertainty in the shell radius, θ_s, is about 4% (ref. [39]), although particular regions could have departures from sphericity larger than that. Added in quadrature, the uncertainties in θ_s and screen location relative to the shell add about 1.0 pc to the uncertainty in z_p, which is small compared to its estimated uncertainty of 5.5 pc. V_z and ζ_v have additional uncertainties related to the uncertainty in the exact location of the pulsar birthplace, but their contributions are also small compared to 87% of the uncertainty from the estimated distance. Although any improvement in the relevant parameters is desirable, improved VLBI astrometry for the pulsar and/or an improved distance estimate for the SNR would be the most valuable.

Regarding possible origins for the (small) misalignment of the spin and velocity vectors for PSR J0538+2817, it is of interest that Dinçel et al.[14] have identified an OB runaway star within SNR S147. The OB star has a proper motion consistent

with an origin at the estimated birth location of PSR J0538+2817 and a 3D velocity that is of opposite sign to the pulsar velocity but with a substantial misalignment. Break-up of a pre-supernova binary system containing this star would have perturbed any pulsar velocity arising from a natal kick.

Modelling of the central bright ridge. The central bright ridge could be caused by instrumental effects, such as fine scale variations in the system bandpass that also vary with time on a scale of ~30 s. However, no ridge is observed in any of several other pulsars observed with the same receiver on FAST and showing clear parabolic arcs. Alternatively, the ridge could represent a collection of high-curvature arcs caused by low-velocity scattering in the SNR or by scattering by a screen nearer to midway along the line of sight. Neither of these is likely because the velocity is dominated by the pulsar proper motion and because scintillation due to a screen along the path would be quenched by the apparent angular size of the pulsar caused by scattering in the SNR shell. Such an arc-ridge structure can also arise if the scattering medium is anisotropic with the transverse velocity aligned with the major axis of the scattering irregularities.

To explain this, we modelled the secondary spectra having arcs with sharp outer edges as a mapping from the brightness distribution $B(\theta_x, \theta_y)$ to the secondary spectrum $S(f_t, f_\nu)$, where

$$f_t = \frac{\theta_x V_x}{\lambda} \text{ and } f_\nu = \frac{(\theta_x^2 + \theta_y^2)Z}{2c}, \tag{27}$$

$$\theta_x = \frac{f_t \lambda}{V_x} \text{ and } \theta_y = \pm\sqrt{\frac{2cf_\nu}{Z} - \left(\frac{f_t \lambda}{V_x}\right)^2}. \tag{28}$$

Here, we assume the velocity is in the x direction. The Jacobian of the transformation is $J = 1/\theta_y$, which has a half-order singularity where $\theta_y = 0$. This singularity is the sharp arc. We have simplified the equations without loss of generality by taking the case of the scattering medium a distance Z from the observer and an infinitely distant source. We can demonstrate this mapping for a Kolmogorov brightness distribution as shown in Extended Data Fig. 5. There, we plotted three cases left to right: isotropic, anisotropic aligned with V and anisotropic perpendicular to V. In these simulations, the anisotropic cases have an axial ratio $A_R = 3$. We have included a phase gradient typical of that in seen in the observed secondary spectra in each simulation. In anisotropic scattering cases, the shape of the primary arc is independent of the anisotropy, but the power distribution inside the arc depends strongly on it. From Extended Data Fig. 5, an axial ratio for the scattering structures of just 3, with the major axis of scattering irregularities (that is, the minor axis of the brightness distribution) aligned with the velocity, results in a central ridge that matches the observations well. Neither the isotropic case nor a perpendicular anisotropy results in a central ridge. For deviations in alignment greater than about 10°, the ridge would be noticeably displaced from the central axis.

Based on the observed value of scintillation timescale at 1,400 MHz, we can derive the spatial scale and the r.m.s. scattering angle in the direction parallel to the velocity:

$$\theta_{par} = \frac{c}{2\pi\nu_c \Delta\tau_d[V_{psr,\perp}(1-s) - V_{scr,\perp}]} = 0.70 \pm 0.10 \text{ mas}. \tag{29}$$

The r.m.s. scattering angle in the perpendicular direction will be $\theta_{perp} = A_R \theta_{par}$, where A_R is the axial ratio of an asymmetric scattering structure. Furthermore, we can use the measured bandwidth to estimate A_R as follows

$$\Delta\nu_d = \frac{1}{2\pi\tau_{sc}} = \frac{c}{\pi D_{ps}(\theta_{par}^2 + \theta_{perp}^2)}, \tag{30}$$

where τ_{sc} is the profile scatter-broadening timescale. Hence,

$$A_R^2 = \frac{c}{\pi\Delta\nu_d \, D_{ps} \, \theta_{par}^2} - 1. \tag{31}$$

Substituting for $\Delta\nu_d \approx 0.86$ MHz and $\theta_{par} \approx 0.70$ mas at 1,400 MHz, we obtain $A_R \approx 3$, which matches well with the above simulation result.

Data availability

The data used in this investigation are available at https://crafts.bao.ac.cn/pub/data/yjm/2021/PSR0538+2817DS.zip. The data that support the plots can be requested from the corresponding authors.

References

1. Hewish, A., Bell, S. J., Pilkington, J. D. H., Scott, P. F. & Collins, R. A. Observation of a rapidly pulsating radio source. *Nature* **217**, 709–713 (1968).

2. Large, M. I., Vaughan, A. E. & Mills, B. Y. A pulsar supernova association?. *Nature* **220**, 340–341 (1968).

3. Comella, J. M., Craft, H. D.Jr, Lovelace, R. V. E., Sutton, J. M. & Tyler, G. L. Crab nebula Pulsar NP 0532. *Nature* **221**, 453–454 (1969).

4. Gold, T. Rotating neutron stars as the origin of the pulsating radio sources. *Nature* **218**, 731–732 (1968).

5. Lyne, A. G. & Lorimer, D. R. High birth velocities of radio pulsars. *Nature* **369**, 127–129 (1994).

6. Janka, H.-T. Neutron star kicks by the gravitational tug-boat mechanism in asymmetric supernova explosions: progenitor and explosion dependence. *Astrophys. J.* **837**, 84 (2017).

7. Powell, J. & Müller, B. Three-dimensional core-collapse supernova simulations of massive and rotating progenitors. *Mon. Not. R. Astron. Soc.* **494**, 4665–4675 (2020).

8. Wongwathanarat, A., Janka, H.-T. & Müller, E. Three-dimensional neutrino-driven supernovae: neutron star kicks, spins, and asymmetric ejection of nucleosynthesis products. *Astron. Astrophys.* **552**, A126 (2013).

9. Müller, B. et al. Three-dimensional simulations of neutrino-driven core-collapse supernovae from low-mass single and binary star progenitors. *Mon. Not. R. Astron. Soc.* **484**, 3307–3324 (2019).

10. Anderson, S. B. et al. A 143 millisecond radio pulsar in the supernova remnant S147. *Astrophys. J.* **468**, L55–L58 (1996).

11. Romani, R. W. & Ng, C.-Y. The pulsar wind nebula torus of PSR J0538+2817 and the origin of pulsar velocities. *Astrophys. J.* **585**, L41–L44 (2003).

12. Kramer, M. et al. The proper motion, age, and initial spin period of PSR J0538+2817 in S147. *Astrophys. J.* **593**, L31–L34 (2003).

13. Chatterjee, S. et al. Precision astrometry with the Very Long Baseline Array: parallaxes and proper motions for 14 pulsars. *Astrophys. J.* **698**, 250–265 (2009).

14. Dinçel, B. et al. Discovery of an OB runaway star inside SNR S147. *Mon. Not. R. Astron. Soc.* **448**, 3196–3205 (2015).

15. Edwards, R. T., Hobbs, G. B. & Manchester, R. N. TEMPO2, a new pulsar timing package - II. The timing model and precision estimates. *Mon. Not. R. Astron. Soc.* **372**, 1549–1574 (2006).

16. Freire, P. C. C. et al. On the nature and evolution of the unique binary pulsar J1903+0327. *Mon. Not. R. Astron. Soc.* **412**, 2763–2780 (2011).

17. Li, D. et al. FAST in space: considerations for a multibeam, multipurpose survey using China's 500-m Aperture Spherical Radio Telescope (FAST). *IEEE Microw. Mag.* **19**, 112–119 (2018).

18. Rickett, B. J. Radio propagation through the turbulent interstellar plasma. *Annu. Rev. Astron. Astrophys.* **28**, 561–605 (1990).

19. Stinebring, D. R. et al. Faint scattering around pulsars: probing the interstellar medium on Solar System size scales. *Astrophys. J.* **549**, L97–L100 (2001).

20. Cordes, J. M., Rickett, B. J., Stinebring, D. R. & Coles, W. A. Theory of parabolic arcs in interstellar scintillation spectra. *Astrophys. J.* **637**, 346–365 (2006).

21. Radhakrishnan, V. & Cooke, D. J. Magnetic poles and the polarization structure of pulsar radiation. *Astrophys. Lett.* **3**, 225–229 (1969).

22. Ng, C.-Y. & Romani, R. W. Fitting pulsar wind tori. *Astrophys. J.* **601**, 479–484 (2004).

23. Noutsos, A., Kramer, M., Carr, P. & Johnston, S. Pulsar spin–velocity alignment: further results and discussion. *Mon. Not. R. Astron. Soc.* **423**, 2736–2752 (2012).

24. Tademaru, E. & Harrison, E. R. Acceleration of pulsars to high velocities by asymmetric radiation. *Nature* **254**, 676–677 (1975).

25. Janka, H.-T., Melson, T. & Summa, A. Physics of core-collapse supernovae in three dimensions: a sneak preview. *Annu. Rev. Nucl. Part. Sci.* **66**, 341–375 (2016).

26. Heger, A., Woosley, S. E. & Spruit, H. C. Presupernova evolution of differentially rotating massive stars including magnetic fields. *Astrophys. J.* **626**, 350–363 (2005).

27. Ng, C.-Y. & Romani, R. W. Birth kick distributions and the spin-kick correlation of young pulsars. *Astrophys. J.* **660**, 1357–1374 (2007).

28. Spruit, H. & Phinney, E. S. Birth kicks as the origin of pulsar rotation. *Nature* **393**, 139–141 (1998).

29. Jiang, P. et al. The fundamental performance of FAST with 19-beam receiver at *L* band. *Res. Astron. Astrophys.* **20**, 064 (2020).

30. van Straten, W. & Bailes, M. DSPSR: digital signal processing software for pulsar astronomy. *Publ. Astron. Soc. Aust.* **28**, 1–14 (2011).

31. van Straten, W., Demorest, P. & Oslowski, S. Pulsar data analysis with PSRCHIVE. *Astron. Res. Technol.* **9**, 237–256 (2012).

32. Coles, W., Hobbs, G., Champion, D. J., Manchester, R. N. & Verbiest, J. P. W. Pulsar timing analysis in the presence of correlated noise. *Mon. Not. R. Astron. Soc.* **418**, 561–570 (2011).

33. Mitra, D., Wielebinski, R., Kramer, M. & Jessner, A. The effect of HII regions on rotation measure of pulsars. *Astron. Astrophys.* **398**, 993–1005 (2003).

34. Lyne, A. G. & Manchester, R. N. The shape of pulsar radio beams. *Mon. Not. R. Astron. Soc.* **234**, 477–508 (1988).

35. Everett, J. E. & Weisberg, J. M. Emission beam geometry of selected pulsars derived from average pulse polarization data. *Astrophys. J.* **553**, 341–357 (2001).
36. Cordes, J. M., Weisberg, J. M. & Boriakoff, V. Small-scale electron density turbulence in the interstellar medium. *Astrophys. J.* **288**, 221–247 (1985).
37. Wang, N. et al. Long-term scintillation observations of five pulsars at 1540 MHz. *Mon. Not. R. Astron. Soc.* **358**, 270–282 (2005).
38. Kirshner, R. P. & Arnold, C. N. Kinematics of supernova remnant S147. *Astrophys. J* **229**, 147–152 (1979).
39. Sofue, Y., Furst, E. & Hirth, W. Radio continuum observations at 5 GHz of the supernova remnant S147. *Publ. Astron. Soc. Jpn* **32**, 1–10 (1980).
40. Chen, B.-Q. et al. Mapping the three-dimensional dust extinction towards the supernova remnant S147 – the S147 dust cloud. *Mon. Not. R. Astron. Soc.* **472**, 3924–3935 (2017).

Author contributions
J.Y. led the project. W.Z., D.L., N.W., J.L. and D.R.S. were involved in discussing the proposal for these observations. P.W. and C.M. helped with data analysis and M.Y. made the two 3D plots. R.N.M., W.Z., W.A.C. and D.L. made major contributions to the preparation of the manuscript. D.R.S. commented on the ISS data analysis, and Y.F., W.Y. and M.K. helped with polarization calibrations. All authors reviewed, discussed and commented on the results and the manuscript.

Competing interests
The authors declare no competing interests.

Additional information
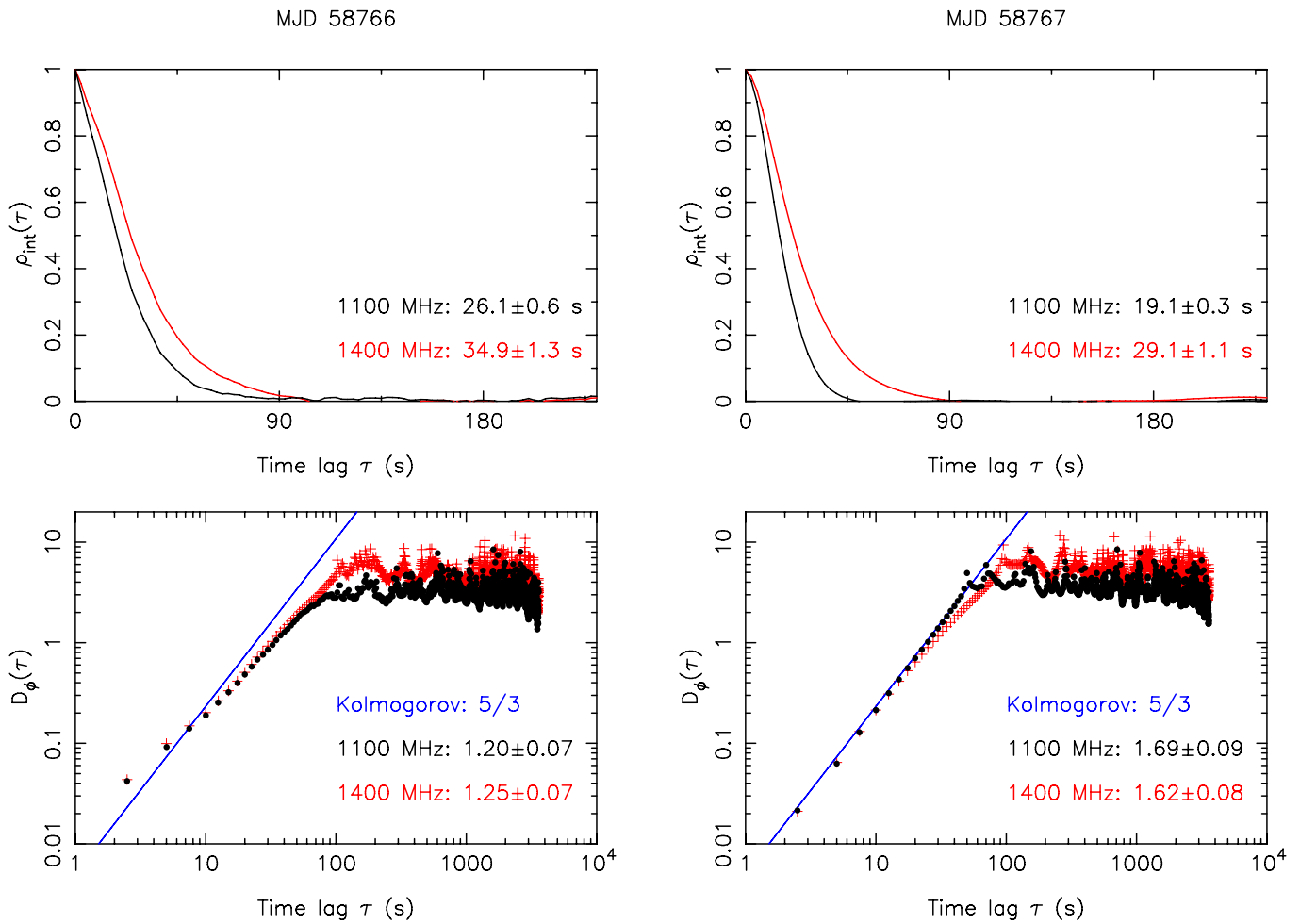**Extended data** is available for this paper at https://doi.org/10.1038/s41550-021-01360-w.

Correspondence and requests for materials should be addressed to J.Y., W.Z. or D.L.

Peer review information *Nature Astronomy* thanks the anonymous reviewers for their contribution to the peer review of this work.
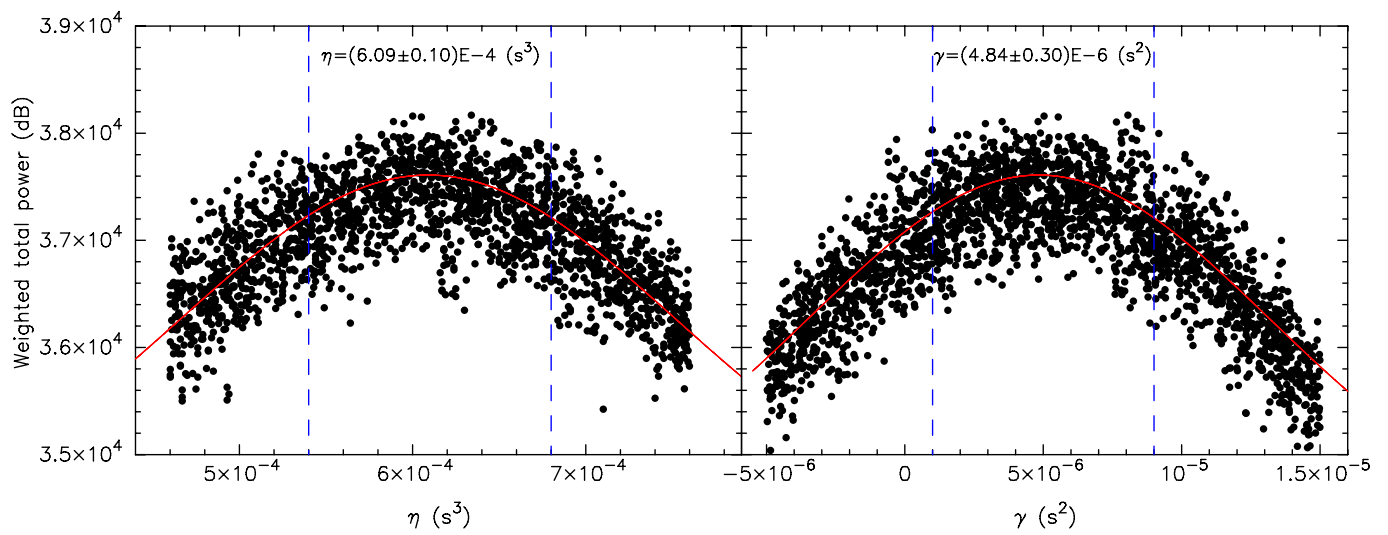
Reprints and permissions information is available at www.nature.com/reprints.

Publisher's note Springer Nature remains neutral with regard to jurisdictional claims in published maps and institutional affiliations.
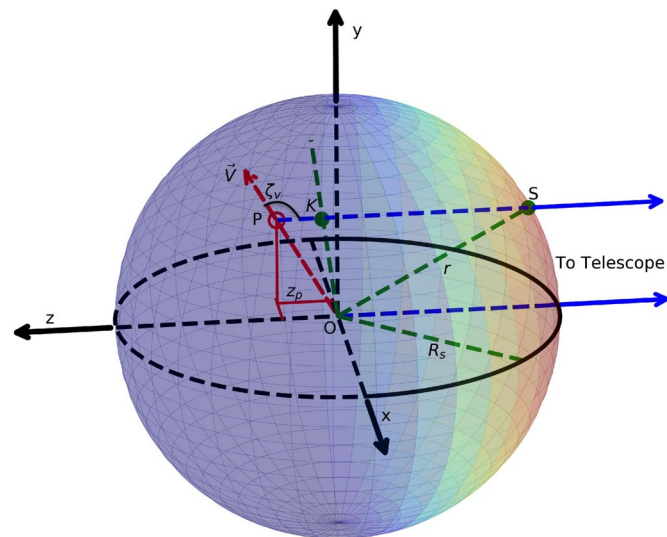
MJD 58766

MJD 58767

Extended Data Fig. 1 | One-dimensional time-domain ACFs for dynamic spectra and the corresponding structure functions. Left panels show the ACF and the structure function for MJD 58766. Right panels show the ACF and the structure function for MJD 58767. The best-fit parameters with 1-σ uncertainties are showed in four panels. To facilitate comparison of the linear parts of the structure functions for the two bands, the D_ϕ axis for the 1,100 MHz structure function has been scaled by $(1,100/1,400)^2$.
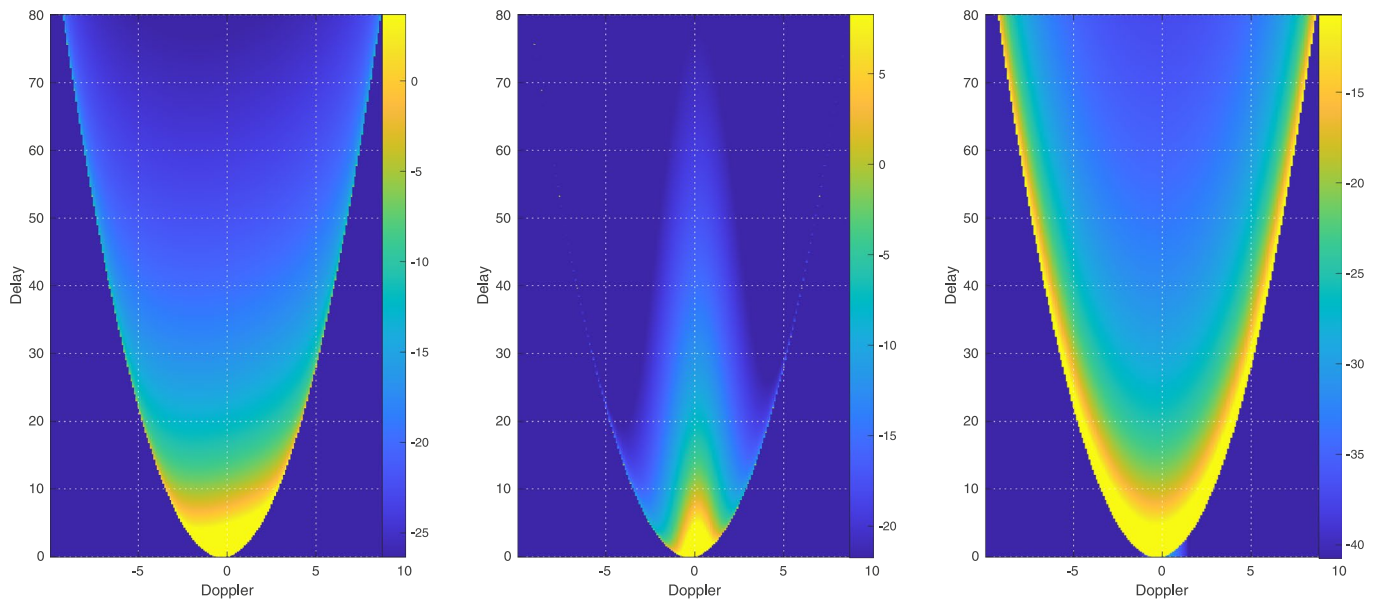
Extended Data Fig. 2 | Distribution of the summed arc power. Left and right panel show the distribution of the summed arc power in the η direction and the γ direction, respectively. The vertical dashed lines delineate the η and γ ranges used for the two-dimensional fit to the power and the plotted points are from within these ranges. The red lines are cuts through the 2D Gaussian fit at the best-fit value of the other coordinate. The Gaussian fit results of η and γ are showed as best-fit value with 1-σ uncertainties.

Extended Data Fig. 3 | The adopted coordinate system for the SNR S147 - PSR J0538+2817 system. The coordinate system is centred at the geometric centre of SNR S147 (O) with the +x axis in the direction of increasing right ascension (E), the +y axis toward north, and the +z axis away from the observer. We mark the current pulsar position as P (x_p, y_p, z_p) and its projection on the x-y plane as K $(x_p, y_p, 0)$, and the scattering screen as S (x_s, y_s, z_s). The inclination of the pulsar velocity $\vec{V}$ to the line of sight is ζ_v, r is the distance of the scattering screen from the origin and the SNR shell radius is R_s.

MJD	Time	η	γ	s	D_{ps}	z_p	ζ_V	V_z	V_{tot}	θ_g
	(min)	(s^3)	(s^2)		(pc)	(pc)	(deg)	(km s^{-1})	(km s^{-1})	(μas)
58635	45	$(6.24\pm0.14)\times10^{-4}$	$(-3.24\pm0.67)\times10^{-6}$	$0.0247^{+0.0043}_{-0.0043}$	$32.9^{+7.4}_{-7.4}$	$3.6^{+5.9}_{-5.6}$	115^{+15}_{-30}	101^{+166}_{-157}	408^{+83}_{-57}	$-8.0^{+1.7}_{-1.7}$
58733	120	$(6.08\pm0.06)\times10^{-4}$	$(3.46\pm0.28)\times10^{-6}$	$0.0241^{+0.0040}_{-0.0040}$	$32.1^{+7.0}_{-7.0}$	$2.9^{+5.5}_{-5.2}$	110^{+16}_{-28}	81^{+154}_{-147}	406^{+78}_{-57}	$8.7^{+0.8}_{-0.8}$
58766	60	$(6.01\pm0.05)\times10^{-4}$	$(1.61\pm0.24)\times10^{-6}$	$0.0238^{+0.0040}_{-0.0040}$	$31.7^{+7.0}_{-7.0}$	$2.5^{+5.5}_{-5.2}$	108^{+17}_{-28}	71^{+154}_{-147}	406^{+77}_{-57}	$4.0^{+0.6}_{-0.6}$
58767	60	$(6.09\pm0.10)\times10^{-4}$	$(4.84\pm0.30)\times10^{-6}$	$0.0241^{+0.0041}_{-0.0041}$	$32.1^{+7.1}_{-7.1}$	$2.9^{+5.6}_{-5.4}$	110^{+16}_{-29}	81^{+158}_{-150}	407^{+79}_{-57}	$12.1^{+0.8}_{-0.8}$

Extended Data Fig. 4 | The value of η and γ and seven parameters derived from 1400 MHz observations at four observational epochs. All quantities are listed as the best-fit value with 1-σ uncertainties.

Extended Data Fig. 5 | Simulated secondary spectra. Isotropic (left); anisotropic aligned with V, as proposed for the observations (centre); anisotropic perpendicular to V (right), with a logarithmic (dB) colour scale. The axial ratio of the anisotropic cases is 3. Each has the same phase gradient, set equal to the value of γ inferred from the observations.